Rotary Coupling Magnetic Field Characteristics of a Two-Degree-of-Freedom Direct Drive Induction Motor

Haichao Feng [1], Jikai Si [2,1], Zhiping Cheng [2], Caixia Gao [1], and Wenping Cao [3]

[1] School of Electrical Engineering and Automation
Henan Polytechnic University, Jiaozuo, 454000, China
fhc@hpu.edu.cn, gcx@hpu.edu.cn

[2] College of Electric Engineering
Zheng Zhou University, Zhengzhou, 450001, China
sijikai527@126.com, zpcheng@zzu.edu.cn

[3] School of Engineering and Applied Science
Aston University, Birmingham, B47ET, UK
w.p.cao@aston.ac.uk

Abstract ─ A two-degree-of-freedom direct drive induction motor is investigated in this study. Owing to its special structure and motion forms, coupling magnetic fields are generated inside the motor, which links with the main magnetic field and results in low speeds and high fluctuations. In this paper, a three-dimensional finite element model of the two-degree-of-freedom direct drive induction motor is developed to determine the rotary coupling magnetic field and its effect on the motor. The distribution of the rotary coupling magnetic field is calculated qualitatively based on a simplified model, and its variation law is investigated based on the changes of the induced voltages in a special coupling model. Moreover, the relationship between the rotary coupling magnetic field and the motor speed is determined by the rotary coupling coefficient. A test platform is applied to verify the coupling model and its results.

Index Terms ─ Coupling magnetic field, induced voltages, three-dimensional finite element model, two-degree-of-freedom.

I. INTRODUCTION

The combination of rotary and linear motions on the same axis is often required in robot arms, diverse industrial and vehicles applications [1-2]. These proposed two-degrees-of-freedom motors (2DoFMs), which are capable of rotary, linear and helical motions through the use of single motors, seems to be an excellent solution.

2DoFMs with different structures have been proposed and investigated in recent years due to their advantages of integrated structures, small volume, and high reliability. To realize special motion forms, 2DoFMs adopt special structures [3-6], such as Halbach structure, multi-stators, and multi-windings. Amiri et al. [5] investigated a two-armature rotary-linear induction motor, which adopted a rotary armature connecting with a linear armature in series to achieve helical motion. Li et al. [7] investigated a decoupled 2DoF in the linear and rotary directions of a motor based on switched reluctance principle. Szabó et al. [8] proposed a rotary-linear switched reluctance motor, in which the armature was constructed with a rotor stack of six common poles mounted on a common shaft. A Halbach magnet array and multi-windings were adopted in a permanent magnetic rotary-linear motor, in which the motion forms were determined by the power supply [9]. However, their major structures and magnetic fields were more complicated than the traditional single-degree-of-freedom motors. Previously, the rotary torque and efficiency of the two-armature rotary-linear induction motor could be weakened to some extent by the linear end magnetic field and motion [10-11]. For the magnetic field modeling and the motor characteristic analysis, the severe magnetic saturation should be accurately predicted [12]. Furthermore, by considering the weakening effect in the form of additional magnetomotive force, the computational accuracy of its equivalent circuit model could be improved, and verified by the finite element results [13]. References [14] presented a three-dimensional (3D) finite element analysis (FEA) applicable to all forms of sheet rotor, cylindrical, linear induction motor, as well as, helical motion induction motor. The linear thrust of the rotary-linear switched reluctance motor with multi rotary stators, which is dependent on the power supply mode, could be generated by the coupling among the stators [15]. For the permanent magnetic rotary-linear motor with Halbach

Submitted On: March 24, 2019
Accepted On: June 27, 2019

magnet array, its circular magnetic field was linked to its axial magnetic field and verified by the static magnetic field solved via the FEA [6]. Furthermore, the interval between two successive magnets in the axial direction could affect the rotary and linear magnetic flux densities [16]. Thus, the special coupling phenomenon, by which the magnetic fields of different degrees of freedom interact with each other, is common in 2DoFMs.

A two-degree-of-freedom direct drive induction motor (2DoFDDIM) was proposed and designed to realize the three motion forms, namely rotary, linear and helical [17]. Owing to the special structure and assembly form of 2DoFDDIM stators, the presence of coupling magnetic fields lead to distinctive features, such as 'super-synchronization' and the static coupling effect, which have been analyzed in references [18] and [19], respectively. The characteristics of the helical motion of the two-degree-of-freedom induction motor were investigated, and a set of torque and force equations of the helical motion were deduced in references [20]. However, these studies do not focus on the origin of these phenomena, and the coupling magnetic field, which should be fully investigated and considered in the design and control system of the motors.

The coupling magnetic fields and their effect on the performances of 2DoFDDIM are determined via a 3D finite element model of the motor. Two forms of coupling magnetic fields exist inside 2DoFDDIM, namely the rotary coupling magnetic field (RCMF) and linear coupling magnetic field (LCMF). In this paper, only the RCMF was mainly investigated. The equation for RCMF was calculated qualitatively based on a simplified model, and its variation law was determined based on the changes of induced voltages in a special coupling model, which was validated via experiments on a prototype coupling motor.

II. STRUCTURE AND COUPLING MAGNETIC FIELD OF 2DoFDDIM

A. Structure and characteristics of 2DoFDDIM

Figure 1 shows the 2DoFDDIM structure, which contains a rotary arc armature in the rotary part, a linear arc armature in the linear part, and a solid copper-coated mover shared by the two parts. Table 1 lists the main parameters of 2DoFDDIM.

On the basis of the power supply mode, 2DoFDDIM produces different forms of air gap magnetic fields, which generate the corresponding electromagnetic force on the mover surface to drive it directly and perform the rotary, linear, or helical motion.

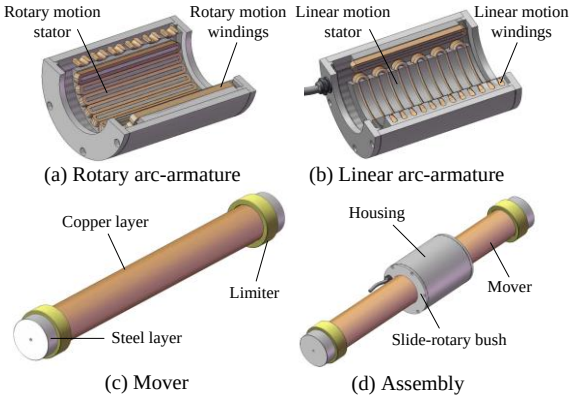

Fig. 1. 2DoFDDIM structure.

Table 1: Main parameters of 2DoFDDIM

Item	Values/Dimension	
	Rotary Part	**Linear Part**
Rated power (P_N)	1.1 kW	1.1 kW
Rated voltage (U_N)	220 V (Y)	220 V (Y)
Rated current	9 A	12 A
Frequency (f)	50 Hz	50 Hz
Pole pair (p)	2	2
Stator inner diameter	98 mm	98 mm
Stator outer diameter	155 mm	155 mm
Stator axial length	135 mm	135 mm
Slots	12	12
Air-gap length	2 mm	2 mm
Mover length	655 mm	
Copper layer thickness of mover	1 mm	
Steel layer thickness of mover	7 mm	

According to the 2DoFDDIM structure shown in Fig. 1 and its working principle, the 3D finite element model of 2DoFDDIM is established in *Magnet*, as shown in Fig. 2.

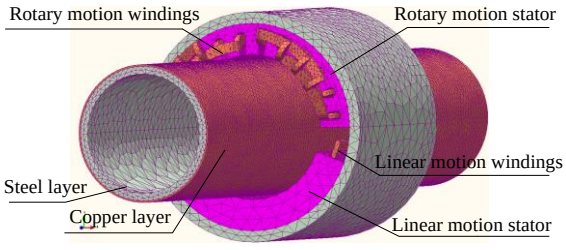

Fig. 2. 3D finite element model of 2DoFDDIM.

Figure 3 shows the torque-slip ratio S_r and force-slip ratio S_l curves of 2DoFDDIM, where S_r and S_l denote the slip ratios in the rotary and linear motions, respectively. Figure 3 (a) presents the torque-S_r curve indicating the mechanical characteristics of the 2D rotary motion of 2DoFDDIM. Rotating torque increased monotonously with the increase in S_r, which was similar to that of the traditional solid-rotor rotary induction motor. Figure 3 (b) shows the force-S_l characteristic of the linear motion of 2DoFDDIM. The increase in S_l increased the force.

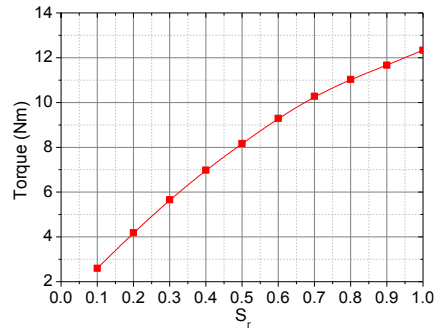

(a) Torque-S_r (Rotary motion)

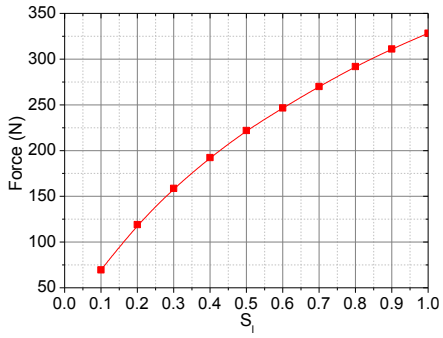

(b) Force-S_l (Linear motion)

Fig. 3. (a) The torque-slip ratio S_r and (b) force-slip ratio S_l characteristics of 2DoFDDIM.

B. Coupling magnetic field of 2DoFDDIM

According to the special structure and the installation mode of the armature of the 2DoFDDIM, when the rotary part or linear part is energized independently, the distribution of the magnetic field is shown in Fig. 4. Figure 4 presents that the 0°-180° area in the circumference belongs to the rotary part, and the other belongs to the linear part according to the 2DoFDDIM structure.

It can be seen from Fig. 4 (a) that the rotary magnetic field will affect the linear part, when only the rotary part of the motor is powered. As shown in Fig. 4 (b), when the motor is only doing linear motion (only linear part is powered), the traveling wave magnetic field in the linear part has an impact on the rotary part.

The magnetic field generated by the rotary part stator and crosslinking in the linear part stator (induced magnetic field in linear part) is defined as rotary coupling magnetic field (RCMF). Similarly, the magnetic field generated by the linear stator and crosslinking in the rotary part stator (induced magnetic field in rotary part) is called the linear coupling magnetic field (LCMF).

Figure 4 illustrates the parts of the magnetic field when 2DoFDDIM performs the single degree of freedom motion as follows:

1) Effective magnetic field, by which the mover is driven to perform a rotary or linear motion.

2) Coupling magnetic field, produced by the rotary or linear part and then links with the relative part.

The comparison of Figs. 4 (a) and 4 (b) indicated that the coupling magnetic fields of the rotary and linear parts were different. The upper and lower sides of the RCMF were almost symmetrical, whereas the left and right sides of the LCMF were almost symmetrical because the RCMF and LCMF were generated by the longitudinal end effect of the rotary part and the end windings of the linear part, respectively.

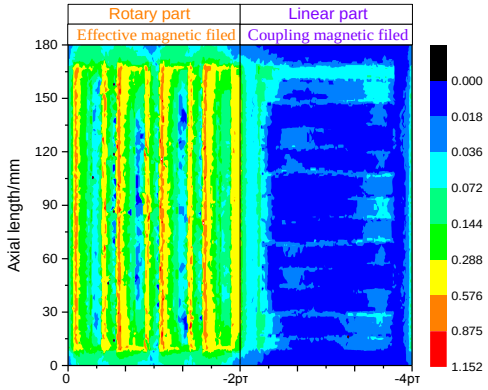

(a) Rotary motion magnetic field
(Only rotary part is powered)

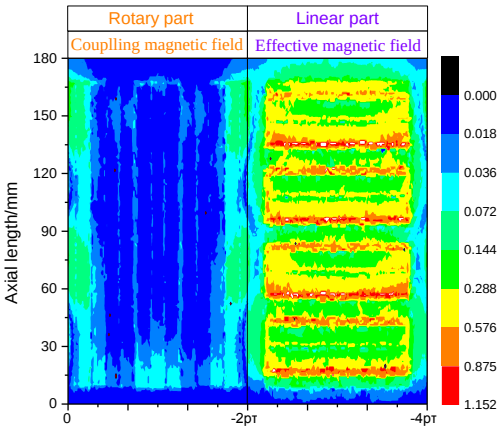

(b) Linear motion magnetic field
(Only linear part is powered)

Fig. 4. Distribution of the air-gap magnetic field of 2DoFDDIM.

C. The effect of coupling magnetic field

Both the rotary and linear parts of 2DoFDDIM can produce the coupling magnetic fields (Fig. 4), which are determined by the cut-off structure of the armature stator cores in the rotary and linear parts and their 2DoFDDIM installation mode. When 2DoFDDIM is under helical motion, coupling magnetic fields still exist and link with the effective magnetic fields. Then, the linear effective magnetic field is taken as an example, and Fig. 5 shows the difference between the linear effective magnetic field with and without the rotary coupling magnetic field.

The comparison of Figs. 5 (a) and 5 (b) indicated that the distribution of the effective magnetic field in the linear part changed in the presence of RCMF. Similarly, the coupling magnetic field in the linear part can also affect the distribution of the effective magnetic field in the rotary part. As the bridge in the conversion of electric to mechanical energy in motors, the effective magnetic field changes will lead to the change in motor performance.

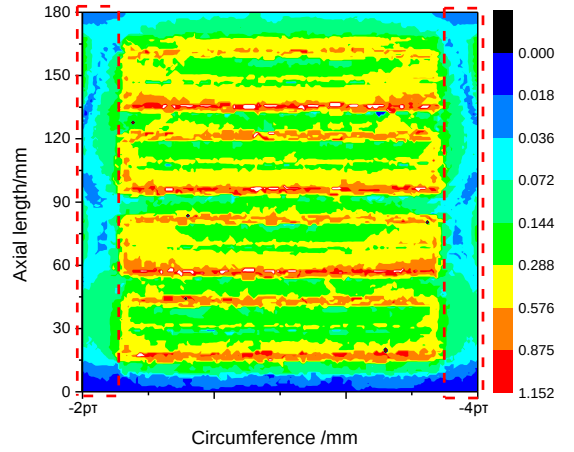

(a) Without rotary coupling magnetic field

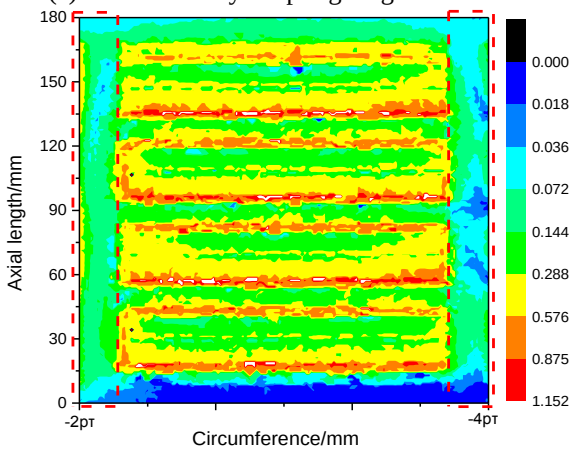

(b) With rotary coupling magnetic field

Fig. 5. Distribution of effective magnetic field in the linear part.

According to the equations in the reference [20], Fig. 6, and Tables 2 and 3 show the influence of the coupling magnetic fields on the output characteristics of the motor based on the 3D finite element model of 2DoFDDIM.

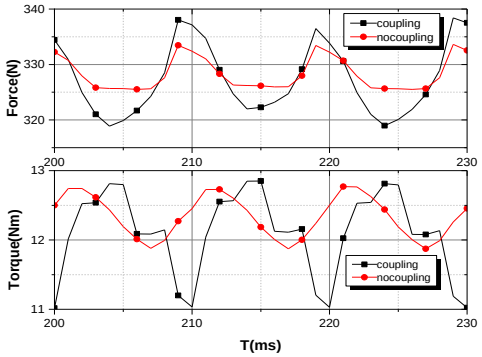

(a) Waveforms of the linear force and rotary torque

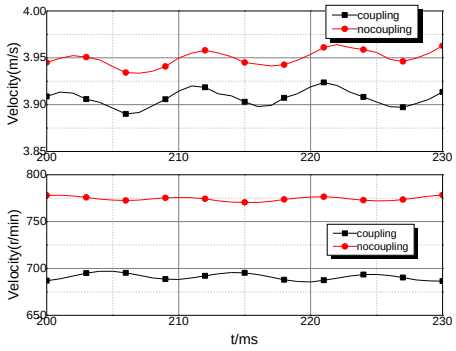

(b) Waveforms of the linear and rotary velocity

Fig. 6. Influence of the coupling magnetic field.

Table 2: Influence of the coupling magnetic field on the linear force and rotary torque

Items		With Coupling	Without Coupling
Rotary part torque	Average (Nm)	12.09	12.34
	Fluctuation(Nm)	0.61	0.30
	Ripple (%)	5.05%	2.43%
Linear part force	Average (N)	327.3	328.3
	Fluctuation (N)	6.236	2.903
	Ripple (%)	1.91	0.88

Table 3: Influence of the coupling magnetic field on the linear and rotary velocity

Items		With Coupling	Without Coupling
Rotary part velocity	Average (r/min)	691	775
	Fluctuation(r/min)	3.35	2.22
	Ripple (%)	0.48	0.29
Linear part velocity	Average (m/s)	3.907	3.949
	Fluctuation (m/s)	0.0086	0.0080
	Ripple (%)	0.22	0.20

Figure 6 (a) and Tables 2 and 3 show that the locked mover torque reduces by 2.03% and the torque fluctuation increases by 104% under the effect of LCMF of 2DoFDDIM. Figure 6 (b) and Table 2 present that the rotary speed reduces by 10.7% and the speed fluctuation increases by 50.9% when compared with that without LCMF. Similarly, similar changes were observed in the performance of the linear part.

Such changes caused by the coupling effect illustrate that the motor performance can be affected by the coupl ing magnetic field. In general, the effect of the coupling magnetic field will lead to low electromagnetic forces a nd speeds and high motor fluctuations.

III. THE COUPLING MAGNETIC FIELD IN THE ROTARY PART

At present, the effect of the coupling magnetic field on the motor's performance has been simply verified by the previous section. The characteristics of the coupling magnetic field should be examined in depth to determine the details on such effect.

In this study, only the RCMF was selected as the research project, whereas the LCMF will be investigated in a corresponding study.

To calculate the rotary coupling magnetic field of 2DoFDDIM, the rotary part was converted into a simplified model (Fig. 7) with the following assumptions.

1) Relative permeability, μ_r, of the arc armature core in the 2DoFDDIM rotary part was infinitely great, and conductivity, γ_r, was infinitely small. Hence, $\mu_r = \infty$, $\gamma_r = 0$.

2) The impact of the linear stator core and slot was ignored, and the magnetic field was deemed uniformly distributed along the axial length. Therefore, such impact had no relation with the Z coordinates while analyzing the coupling magnetic field in the rotary part.

3) The stator and the mover were spread; thus, the armature and mover curvature were ignored, respectively.

4) The three-phase symmetrical sinusoidal current was connected to the armature winding, and all the electromagnetic volumes were characterized by sinusoidal variation.

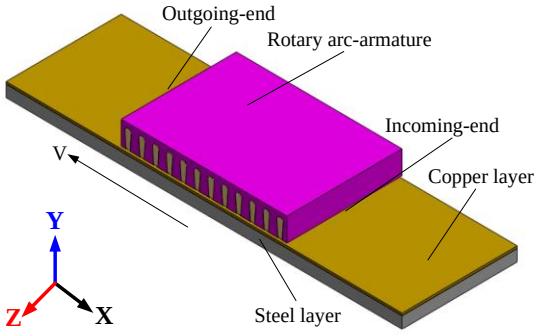

Fig. 7. Equivalent coupling magnetic field model.

The following equations define the vector magnetic potential:

$$\begin{cases} \nabla^2 \dot{A}_{mx} - j\mu_0\gamma\omega_1\dot{A}_{mx} = -\mu_0\dot{J}_{mx} \\ \nabla^2 \dot{A}_{my} - j\mu_0\gamma\omega_1\dot{A}_{my} - \mu_0\gamma v\left(\dfrac{\partial A_{my}}{\partial x} - \dfrac{\partial A_{mx}}{\partial y}\right) = -\mu_0\dot{J}_{my}, \\ \nabla^2 \dot{A}_{mz} - j\mu_0\gamma\omega_1\dot{A}_{mz} - \mu_0\gamma v\left(\dfrac{\partial A_{mz}}{\partial x} - \dfrac{\partial A_{mx}}{\partial z}\right) = -\mu_0\dot{J}_{mz} \end{cases} \quad (1)$$

where $\dot{A}_{mx}, \dot{A}_{my}, \dot{A}_{mz}$ denote the complex amplitude of the vector magnetic potential in the *x*, *y*, and *z* directions, respectively, and $\dot{1}_x\dot{A}_{mx} + \dot{1}_y\dot{A}_{my} + \dot{1}_z\dot{A}_{mz} = \dot{A}_m$; $\dot{J}_{mx}$, $\dot{J}_{my}$, $\dot{J}_{mz}$ refer to the electrical current density $\dot{J}_m$ in the *x*, *y*, and *z* directions, respectively; μ_0 indicates the vacuum permeability; γ represents the relative electrical conductivity of the mover; ω_1 refers to the angular frequency; and *v* denotes the rotary speed of the mover.

The above coupling magnetic field model and assumed conditions indicated that $\dot{A}_{mx} = \dot{A}_{mz} = 0$ and $\dot{A}_m = \dot{A}_{my}$. When only the rotary part was powered in the system, electrical current density in the coupling magnetic field will be $\dot{J}_m = 0$. When they are substituted into the equation set of the vector magnetic potential (1), the vector magnetic potential in the coupling magnetic field region can be derived as:

$$\frac{d^2\dot{A}_m}{d^2x^2} - j\mu_0\gamma\omega_1\dot{A}_m - \mu_0\gamma v\frac{d\dot{A}_m}{dx} = 0. \quad (2)$$

The general solution of Equation (2) is:

$$\dot{A}_m = \dot{C}_1 e^{(\lambda_2+\eta_2)\alpha x} + \dot{C}_2 e^{-(\lambda_2-\eta_2)\alpha x}, \quad (3)$$

$$\begin{cases} \eta_2 = (\mu_0\gamma v)/\alpha \\ \lambda_2 = \sqrt{\eta_2^2 + jG}\dot{A}_m, \\ G = \mu_0\gamma\omega_1\alpha^2 \\ \gamma = \gamma_2\Delta/\delta \end{cases} \quad (4)$$

where $\dot{C}_1$ and $\dot{C}_2$ denote the complex constants of the integrals to be confirmed, $\alpha=\pi/\tau$, τ refers to the equivalent pole pitch of the rotating part, γ_2 represents the conductivity of the mover, δ indicates the equivalent electromagnetic air gap, and Δ denotes the thickness of the conductor plant of the mover.

According to the vector magnetic potential in the region of the outgoing-end of the mover, $\dot{A}_{mo}\big|_{x=\infty} = 0$, it can be obtained that:

$$\begin{cases} \dot{C}_1 = 0 \\ \dot{A}_{mo} = \dot{C}_2 e^{-\left(\sqrt{\eta_2^2+jG}-\eta_2\right)\alpha x}, \end{cases} \quad (5)$$

where $0 \le x \le 2p\tau$.

According to the vector magnetic potential in the region of the incoming-end of the mover, $\dot{A}_{mi}\big|_{x=-\infty} = 0$, it

can be obtained that:

$$\begin{cases} \dot{C}_2 = 0 \\ \dot{A}_{mi} = \dot{C}_1 e^{-\left(\sqrt{\eta_2^2 + jG} + \eta_2\right)\alpha x} \end{cases}, \tag{6}$$

where $-4p\tau \le x \le -2p\tau$.

Given that the simplified model was obtained by using an equivalent plate model of the 2DoFDDIM, the vector magnetic potential in the coupling magnetic field was the superposition of the vector magnetic potential in the outgoing and incoming ends. Thus, the complex amplitude of the vector magnetic potential in the coupling magnetic field can be expressed as follows:

$$\begin{aligned} \dot{A}_m &= \dot{A}_{mi} + \dot{A}_{mo} \\ &= \dot{C}_1 e^{\left(\sqrt{\eta_2^2 + jG} + \eta_2\right)\alpha(x - 4p\tau)} + \dot{C}_2 e^{\left(\sqrt{\eta_2^2 + jG} - \eta_2\right)\alpha x}, \end{aligned} \tag{7}$$

where $0 \le x \le 2p\tau$.

Therefore, the magnetic flux density of the coupling magnetic field B_m can be calculated according to $B_m = \partial \dot{A}_m / \partial x$, as shown in Equation (6):

$$B_m = \dot{C}_1 m_1 e^{m_1(x - 4p\tau)} - \dot{C}_2 m_2 e^{-m_2 x}, \tag{8}$$

where:

$$\begin{cases} m_1 = \sqrt{\mu_0^2 \gamma^2 v^2 + j\dfrac{\mu_0 \omega_1 \gamma_2 \Delta}{\delta}} + \mu_0 \gamma v \\ m_2 = \sqrt{\mu_0^2 \gamma^2 v^2 + j\dfrac{\mu_0 \omega_1 \gamma_2 \Delta}{\delta}} - \mu_0 \gamma v \end{cases}.$$

Replace x to θ through coordinate conversion, and the equation becomes:

$$B_m = \dot{C}_1 m_1 e^{m_1(\theta - 2\pi)} - \dot{C}_2 m_2 e^{-m_2 \theta}, \tag{9}$$

where $0 \le \theta \le \pi$.

Equation (9) shows that the rotary coupling magnetic field of 2DoFDDIM is a complicated function related to the position θ, velocity of the mover v, and equivalent electromagnetic air gap δ.

Given that the above equation was derived based on certain assumptions, its computational accuracy was not as high as that of FEA. However, this equation can provide guidance for the research on the variation law of RCMF.

IV. CHARACTERISTICS OF THE COUPLING MAGNETIC FIELD

RCMF also needs specialized magnetic measuring methods combined with the guidance of the equation for accurate measurement. The magnetic field can be measured by using the superconducting magnetic measurement, induction coil, fluxgate, and Hall device [21]. The induction coil is a simple method to measure the magnetic field based on Friday's law of electromagnetic induction. Induction coil exposed to alternating magnetic fields will generate the induced voltage between both of its ends. If the parameters of the induction coil are constant, then the large induced voltage strengthens the magnetic field. In addition, induction coil and the magnetic field can be modeled and simulated through finite element software *Magnet*. Therefore, a special coupling model was proposed and designed in *Magnet* to measure the RCMF by using the induction coil.

A. The coupling model

The special coupling model was established in *Magnet* to calculate the variation of the rotary coupling magnetic field of 2DoFDDIM (Fig. 8 (a)). Figure 8 (b) shows the structure and distribution of the coupling model coils. The coupling model consisted of a rotary arc armature, a solid rotor, and a magnetic field measuring device. The magnetic field measurement device was composed of an iron core and six sets of induction coils with the same structural parameters. Accordingly, the value of the induction voltage at both ends of the induction coils could reflect the intensity of the coupling magnetic field at the coil position, and the change of the induced voltage at both ends of the same induction coil could indicate the variation of the intensity of the coupling magnetic field in this position.

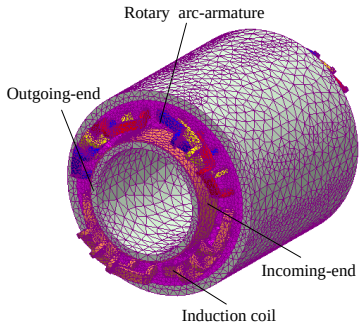

(a) Finite element model

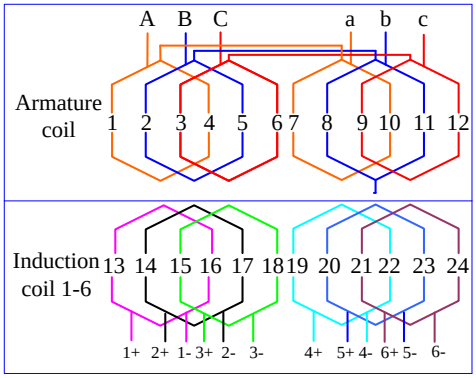

(b) Structure and distribution of coils of the coupling model

Fig. 8. Finite element model and structure of the analysis on the coupling magnetic field.

B. Finite element analysis

To output the same magnetomotive force and reduce the impact on the variables, the coupling model was driven by a current source. When a three-phase sinusoidal alternating current of 14 A was connected with the rotary arc armature of the coupling model, induced voltages could be obtained in the induction coils (Fig. 9).

Figure 9 (a) shows that the induced voltages possess the same frequency as the coupling magnetic field and power source. Furthermore, the induced voltages of induction coils (from coils 1 to 6) decreased first and then increased (Fig. 9 (b)), and the induced voltage of coil 1 was higher than that of coil 6. The above phenomenon illustrated that the RCMF decreased first and then increased from the outgoing end to the incoming end, and the magnetic field in the outgoing end as stronger than that in the incoming end. This phenomenon was consistent with the distribution of the coupling magnetic field in the region from 180°-360° shown in Fig. 4.

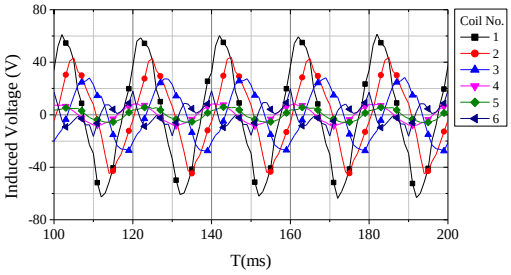

(a) Curves of induced voltages

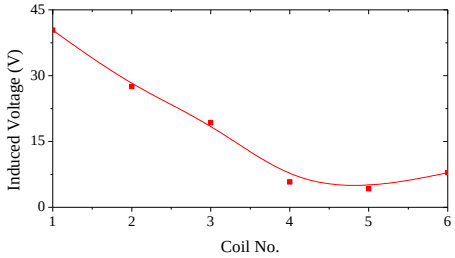

(b) Effective value of induced voltages

Fig. 9. Induced voltages in the induction coils.

RCMF was affected by the rotary speed and the equivalent electromagnetic air gap, and the equivalent electromagnetic air gap was determined by the thickness of the physical air gap and the conductor plate (Fig. 10).

Figure 10 (a) presents the variation of the induced voltages along with the rotary slip. Figures 10 (b) and 10 (c) illustrate the variation of induced voltages under different thickness of the physical air gap and the conductor plate, respectively.

The induced voltages from coils 1 to 6 decreased first and then increased (Fig. 10), thereby indicating that the RCMF decreased first and then increased from the outgoing to the incoming end, and the magnetic field in the outgoing end was stronger than that in the incoming end, which can be considered a general characteristic of the RCMF. Furthermore, the induced voltages decreased generally along with the rotary slip, air gap, and conductor plate thickness, thereby reflecting the general intensity of the decreasing RCMF with the increase in these factors. Moreover, RCMF in the outgoing end reduced more than that in the incoming end with these factors.

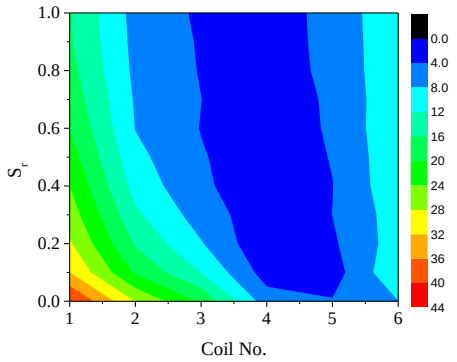

(a) Induced voltages *vs.* rotary slip ratio S_r

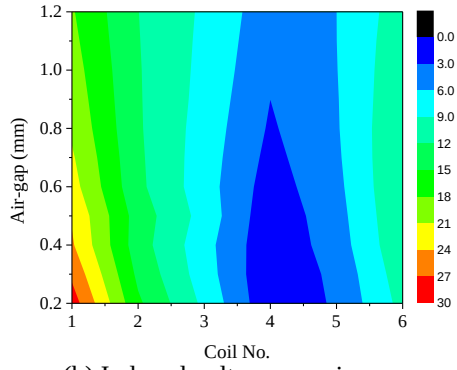

(b) Induced voltages *vs.* air-gap

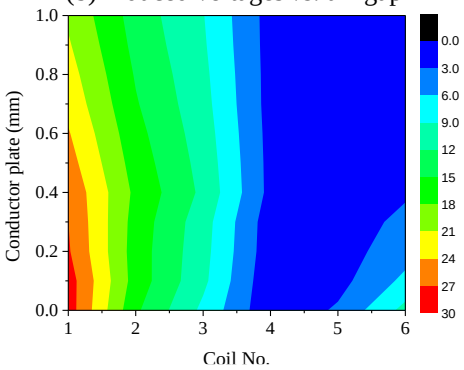

(c) Induced voltages *vs.* conductor plate

Fig. 10. Variations of the induced voltages.

However, RCMF varied along with the rotary slip, air gap, and conductor plate thickness. The comparison of the induced voltage changes of coil 1 in the three figures indicated that its variation along with the rotary slip was higher than that of the other factors. This finding

shows that the coupling magnetic field was significantly affected by the rotary slip.

Both the increase in air gap and conductor plate thickness can change the equivalent electromagnetic air gap and lead to high reluctance. However, the induced voltages of coils 1-3 were decreasing faster than the conductor plate with the increase in air gap. Moreover, the induced voltages of coils 4-6 slowly increased with the increase in air gap but decreased with the increase in conductor plate. Therefore, the corresponding coupling magnetic field demonstrated a similar changing trend with the induced voltages.

C. Rotary coupling coefficient

Section II-C presents that coupling magnetic field has a decreased effect on the motor speed. Additionally, RCMF is variable with the rotary speed, which can be concluded from Section IV-B. To measure the effect of RCMF on linear speed, the following rotary coupling coefficient, K_{rcm}, was introduced:

$$K_{rcm} = V_{lm} / V_{lcm}, \tag{10}$$

where V_{lcm} and V_{lm} express the linear speed of 2DoFDDIM with or without the effect of RCMF, respectively.

Based on the finite element model of 2DoFDDIM shown in Fig. 2, the linear speeds in the presence and absence of RCMF were first measured. Then, the rotary coupling coefficient was calculated and its variation along with rotary slip was shown in Fig. 11.

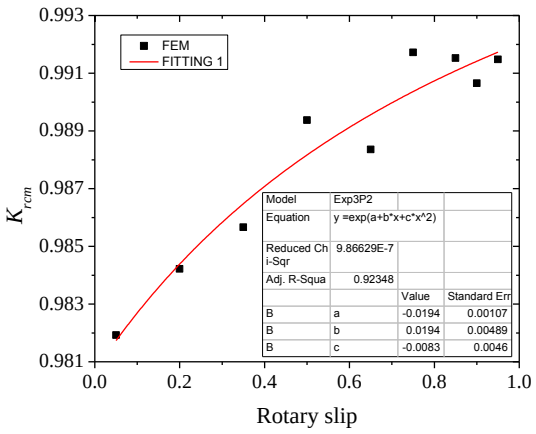

Fig. 11. Fitting curve of rotation coupling coefficient.

By applying curve fitting, the relationship between the rotary coupling coefficient and slip can be obtained as follows:

$$K_{rcm} = e^{-0.0194+0.01943S-0.00838S^2}. \tag{11}$$

From the finite element results in Fig. 11 and Equation (11), the rotary coupling coefficient gradually became close to 1 with increasing rotary slip. This result shows that the effect of RCMF on motor performance decreased with the increase in rotary slip. Section IV-B demonstrates that the general RCMF weakens with the increase in rotary slip. Hence, the effect of coupling magnetic field on motor performance was proportional to its intensity.

Future works include the mathematical model and control system, in which the rotary coupling coefficient should be considered to enhance their precision.

V. EXPERIMENTAL VERIFICATION

To verify the FEA of the rotary coupling magnetic field carried out above, a prototype was manufactured and its main parameters were listed in Table 4. Figure 12 shows the test platform for coupling model prototype.

Table 4: Main parameters of the experimental prototype

Item		Values
Stator inner diameter		98 mm
Stator outer diameter		155 mm
Axial length		135 mm
Slots		24
Armature coil	Phase	3
	Turns	90
Induction coil	Number	6
	Turns	90
Air-gap length		2 mm
Copper layer thickness of mover		1 mm
Steel layer thickness of mover		7 mm

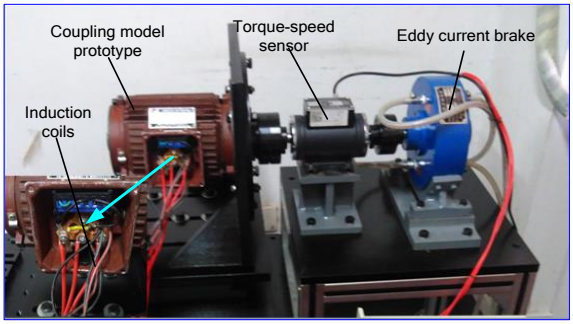

(a) Prototype of the coupling model

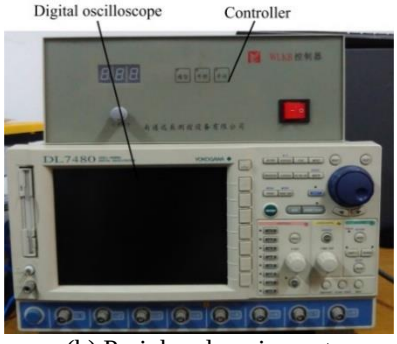

(b) Peripheral equipment

Fig. 12. Platforms and equipment used to conduct prototype experiment of the coupling model.

The test platform for the coupling model prototype included the following: coupling model prototype, torque-speed sensor, eddy current brake, controller, upper computer, and digital oscilloscope. The structure of the coupling model prototype and the distribution of the coils were the same as the coupling model in *Magnet.* The windings were charged with the three-phase AC source, and then the induced voltages could be measured by the digital oscilloscope from the induction coils.

The controller could adjust the output load of the eddy current break by controlling the input current. Then, the speed of the prototype could be controlled by adjusting the load supply and acquired from the upper computer through the torque-speed sensor. The variation of induced voltages along with speed could be measured. Considering safety in the experiment, the slip of the coupling model prototype was set between 0 and 0.5. The induced voltage waveforms measured by the digital oscilloscope are shown in Fig. 13 (a). At the same time, the comparison of finite element and experimental results are shown in Fig. 13 (b).

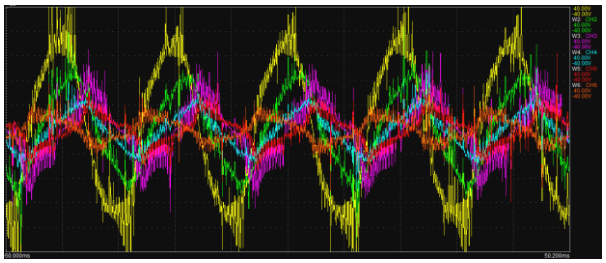

(a) Induced voltage waveform

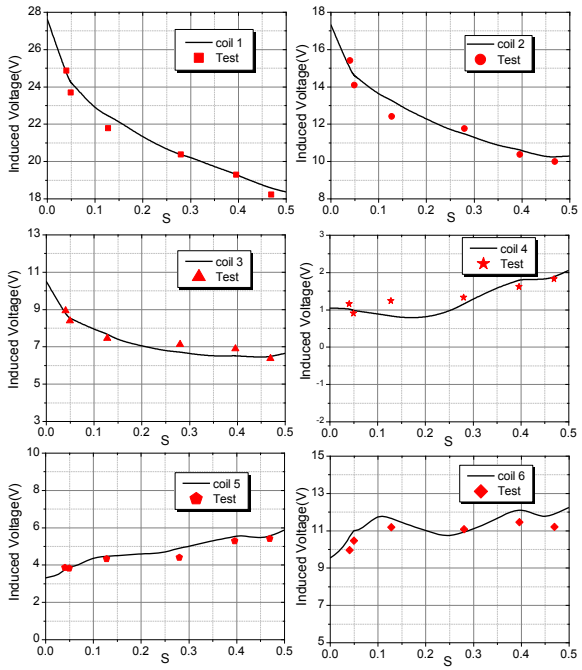

(b) Experimental and finite element results

Fig. 13. Comparison of experiment and FEA results.

The induced voltage waveforms in Fig. 13 (a) were roughly the same as that in Fig. 9 (a). Figure 13 (b) shows that the finite element results are basically the same as the induced voltages measured by the experiment and the variation of the induced voltage as the speed changes. This finding verified the feasibility and correctness of the coupling model of the rotary part. Furthermore, the application of the induced voltage in analyzing the variation of the coupling magnetic field was also validated.

VI. CONCLUSION

As part of the origin of the coupling effect in 2DoFDDIM, the rotary coupling magnetic field is mainly explored and investigated. Through a simplified model of the rotary part, the equation for calculating the RCMF is derived to provide guidance for research on its characteristics. Its variation law with the rotary slip, air gap, and conductor plate thickness is determined based on the special coupling model in *Magnet*. The results show that 2DoFDDIM has the following features:

1) The coupled magnetic field of 2DoFDDIM is caused by the breaking of stator cores in the rotary and linear parts and the mounting method of the stator. The rotary and linear coupling magnetic fields re caused by the longitudinal end effect of the rotating part and the transverse end effect and end winding, respectively.

2) From the view of the rotary coupling magnetic field, the coupling magnetic field in the outgoing end is stronger than that in the incoming end but weakened as the distance between the longitudinal ends of the stator increases.

3) The rotary coupled magnetic field will increase with the increase in velocity and decrease in air gap thickness, which is greatly affected by velocity and minimally affected by air gap thickness.

This research will be considered in future studies that include the development of the precise control of the helical motion and the construction of a mathematical model for the entire motor in the study.

ACKNOWLEDGMENT

The authors thank the National Science Foundation of China under Grant No. 51777060 and No. 51277054, and the Henan Natural Science Foundation of China under Grant No. 162300410117 for supporting this work.

REFERENCES

[1] Y. Sato, "Development of a 2-degree-of-freedom rotational/linear switched reluctance motor," *IEEE Transactions on Magnetics*, vol. 43, no. 6, pp. 2564-2566, June 2007.

[2] S. Y. Li and K. WE. Cheng, "A new two-degree of freedom switched reluctance motor for electric vessel," *In Proceedings of 2015 6th International Conference on Power Electronics Systems and*

Applications (PESA), Hong Kong, pp. 1-6, Dec. 2015.

[3] P. Bolognesi, O. Bruno, F. Papini, V. Biagini, and L. Taponecco, "A low-complexity rotary-linear motor useable for actuation of active wheels," *In Proceedings of 2010 International Symposium on Power Electronics, Electrical Drives, Automation and Motion (SPEEDAM)*, Pisa, Italy, pp. 331-338, June 2010.

[4] M. M. Nezamabadi, E. Afjei, and H. Torkaman, "Design and electromagnetic analysis of new rotary-linear switched reluctance motor in static mode," *Applied Computational Electromagnetics Society Journal*, vol. 31, no. 2, pp. 171-179, Feb. 2016.

[5] E. Amiri, P. Gottipati, and E. A. Mendrela, "3-D space modeling of rotary-linear induction motor with twin-armature," *In Proceedings of 2011 1st International Conference on Electrical Energy Systems (ICEES)*, Tamilnadu, India, pp. 203-206, Jan. 2011.

[6] P. Jin, Y. Yuan, and G. Jian, "Static characteristics of novel air-cored linear and rotary halbach permanent magnet actuator," *IEEE Transactions on Magnetics*, vol. 50, no. 2, pp. 977-980, Feb. 2014.

[7] S. Y. Li, K. W. Cheng, N. Cheung, and Y. Zou, "Design and control of a decoupled rotary-linear switched reluctance motor," *IEEE Transactions on Energy Conversion*, vol. 33, no. 3, pp. 1363-1371, Sep. 2018.

[8] L. Szabó, I. Benţia, and M. Ruba, "A rotary-linear switched reluctance motor for automotive applications," *In Proceedings of 2012 20th International Conference on Electrical Machines (ICEM)*, Marseille, France, pp. 2615-2621, Sep. 2012.

[9] P. Jin, H. Lin, and S. Fang, "Decoupling control of linear and rotary permanent magnet actuator using two-directional d-q transformation," *IEEE Transactions on Magnetics*, vol. 48, no. 10, pp. 2585-2591, Oct. 2012.

[10] O. Dobzhanskyi, E. Amiri, and R. Gouws, "Comparison analysis of electric motors with two degrees of mechanical freedom: PM synchronous motor vs induction motor," *In Proceedings of 2016 2nd International Young Scientists Forum on Applied Physics and Engineering (YSF)*, Kharkiv, Ukraine, pp. 14-17, Oct. 2016.

[11] E. Amiri, M. Jagiela, O. Dobzhanski, and E. Mendrela, "Modeling dynamic end effects in rotary armature of rotary-linear induction motor," *In Proceedings of 2013 IEEE International Electric Machines and Drives Conference (IEMDC)*, Chicago, IL, United States, pp. 1088-1091, May 2013.

[12] S. L. Hu and S. G. Zuo, "Analytical modeling of magnetic field considering the saturation in switched reluctance motor," *Applied Computational Electromagnetics Society Journal*, vol. 33, no. 12, pp. 1467-1474, Dec. 2018.

[13] E. Amiri, "Circuit modeling of double-armature rotary-linear induction motor," *In Proceedings of 2014 40th Annual Conference of the IEEE Industrial Electronics Society (IECON)*, pp. 431-436, Feb. 2014.

[14] J. H. Alwash and L. J. Qaseer, "Three-dimension finite element analysis of a helical motion induction motor," *Applied Computational Electromagnetics Society Journal*, vol. 25, no. 8, pp. 703-712, Aug. 2010.

[15] I. Benţia, M. Ruba, and L. Szabó, "On the control of a rotary-linear switched reluctance motor," *In Proceedings of 2011 5th International Symposium on Computational Intelligence and Intelligent Informatics (ISCIII)*, Floriana, Malta, pp. 41-46, Sep. 2011.

[16] S. Tanaka, T. Shimono, and Y. Fujimoto, "Optimal design of length factor for cross-coupled 2-DOF motor with halbach magnet array," *In Proceedings of 2015 IEEE International Conference on Mechatronics (ICM)*, Nagoya, Japan, pp. 529-534, Mar. 2015.

[17] J. K. Si, H. C. Feng, and L. W. Ai, "Design and analysis of a 2-DOF split-stator induction motor," *IEEE Transactions on Energy Conversion*, vol. 30, no. 3, pp.1200-1208, Sep. 2015.

[18] J. K. Si, L. J. Xie, and X. Z. Xu, "Static coupling effect of a two-degree-of-freedom direct drive induction motor," *IET Electric Power Applications*, vol. 11, no. 4, pp. 532-539, 2017.

[19] J. K. Si, L. W. Ai, and J. B. Han, "Characteristic analysis of no-load speed of linear induction motor," *Dianji yu Kongzhi Xuebao/Electric Machines and Control*, vol. 18, no. 7, pp. 37-43, July 2014.

[20] L. J. Xie, J. K. Si, Y. H. Hu, and H. C. Feng, "Helical motion analysis of the 2-degree-of-freedom split-stator induction motor," *IEEE Transactions on Magnetics*, vol. 55, no. 6, Article Sequence Number: 8103705, June 2019.

[21] Q. J. Pan, W. M. Ma, and Z. H. Zhao, "Development and application of measurement method for magnetic field," *Diangong Jishu Xuebao/ Transactions of China Electrotechnical Society*, vol. 20, no. 3, pp. 1-3, Mar. 2005.

Haichao Feng was born in China in 1983. He received B.S. and M.S. degrees in Electrical Engineering and Automation, Control Theory and Control Engineering from School of Electrical Engineering and Automation, Henan Polytechnic University, China, in 2005 and 2008, respectively. He is currently an Associate Professor and Doctor of Philosophy in Henan Polytechnic University. His research interests are the optimization design of linear and rotary machines, power electronics, and their controls.

Jikai Si received the B.S. degree in Electrical Engineering and Automation from the Jiaozuo Institute of Technology, Jiaozuo, China, in 1998; the M.S. degree in Electrical Engineering from Henan Polytechnic University, Jiaozuo, China, in 2005; and the Ph.D. degree in 2008 from the School of Information and Electrical Engineering, China University of Mining and Technology, Xuzhou, China, in 2008. He is currently a Distinguished Professor at Zhengzhou University. His main research interests include the theory, application, and control of special motor. He has authored and co-authored over 100 technical papers in these areas. Dr. Si is a Member of the Institute of Linear Electric Machine and Drives, Henan Province, China.

Zhiping Cheng was born in China in 1974. He received M.S. degree in Control Theory and Control Engineer from School of Electrical Engineering and Automation, Henan Polytechnical University, China, in 2003. He is currently an Associate Professor in Zhengzhou University, China. His research interests are linear motor and its control.

Caixia Gao was born in China in 1981. She received B.S. and M.S. degrees in Electrical Engineering and Automation, Control Theory and Control Engineering from the School of Electrical Engineering and Automation, Henan Polytechnic University, China, in 2003 and 2008, respectively. She is currently an Associate Professor with Henan Polytechnic University. Her research interests are electrical automation, artificial intelligence and industrial process control.

Wenping Cao received the B.Eng. degree in Electrical Engineering from Beijing Jiao-tong University, China, in 1991, and the Ph.D. degree in Electrical Machines and Drives from the University of Nottingham, U.K., in 2004. He is currently a Professor with Aston University, U.K. His research interests include thermal performance of electric machines, drives and power electronics.